Available online at www.sciencedirect.com
ScienceDirect
International Journal of Heat and Mass Transfer 50 (2007) 1737–1749
International Journal of HEAT and MASS TRANSFER
www.elsevier.com/locate/ijhmt

Thermal contact resistance between plasma-sprayed particles and flat surfaces

André McDonald [a], Christian Moreau [b], Sanjeev Chandra [a,*]

[a] Center for Advanced Coatings Technology, Department of Mechanical and Industrial Engineering, University of Toronto, Toronto, Ontario, Canada M5S 1A4
[b] National Research Council Canada, Industrial Materials Institute, Boucherville, Québec, Canada J4B 6Y4

Received 22 June 2006; received in revised form 13 October 2006
Available online 18 December 2006

Abstract

Plasma-sprayed molybdenum and yttria-stabilized zirconia particles (38–63 μm diameters) were sprayed onto glass and Inconel 625 held at either room temperature or 400 °C. Samples of Inconel 625 were also preheated for 3 h, and then air-cooled to room temperature before spraying. Photographs of the splats were captured by using a fast charge-coupled device (CCD) camera. A rapid two-color pyrometer was used to collect thermal radiation from the particles during flight and spreading to follow the evolution of their temperature. The temperature evolution was used to determine the cooling rate of spreading particles. An analytical heat conduction model was developed to calculate the thermal contact resistance at the interface of the plasma-sprayed particles and the surfaces from splat cooling rates. The analysis showed that thermal contact resistance between the heated or preheated surfaces and the splats was more than an order of magnitude smaller than that on non-heated surfaces held at room temperature. Particles impacting on the heated or preheated surfaces had cooling rates that were significantly larger than those on surfaces held at room temperature, which was attributed to smaller thermal contact resistance.

Keywords: Thermal spray coating; Cooling rate; Non-dimensional temperature; Heat conduction; Splat–substrate interface; Two-color pyrometry

1. Introduction

Substrate temperature has been shown to influence the size and morphology of splats formed by molten particles impacting and solidifying during a thermal spray coating process [1–4]. Droplets of molten zirconia, plasma sprayed onto a stainless steel substrate kept at room temperature, splashed and produced fragmented splats, whereas on a heated substrate they formed circular, disk-like, splats with almost no splashing [5]. Since irregular splats produce porous coatings with poor adhesion strength [6], knowing the causes of droplet splashing is of considerable practical importance.

Pasandideh-Fard et al. [1] used a three-dimensional computational model to simulate the impact and solidification of plasma-sprayed nickel particles on stainless steel substrates and obtained splat shapes that closely resembled those observed in experiments. Splashing was found to occur when the edges of impinging droplets began to freeze; the solidified layer destabilized the outward spreading liquid, making it jet off the substrate and fragment. Simulations showed that reducing the droplet cooling rate and delaying the onset of solidification suppressed splashing. Raising substrate temperature by the amount done in experiments, though, had relatively little effect on heat transfer; varying thermal contact resistance between the substrate and droplet had a much more significant impact on droplet impact dynamics. The explanation offered [1,6] was that heating the steel surface produces an oxide layer that increases contact resistance. This – more than the

* Corresponding author. Tel.: +1 416 978 5742; fax: +1 416 978 7753.
E-mail address: chandra@mie.utoronto.ca (S. Chandra).

0017-9310/$ - see front matter © 2006 Elsevier Ltd. All rights reserved.
doi:10.1016/j.ijheatmasstransfer.2006.10.022

Nomenclature

A	splat area (m^2)
Bi	Biot number, $Bi = h/R_c k_s$
D	splat diameter (m)
Fo	Fourier number, $Fo = \alpha t/h^2$
h	splat thickness at the maximum extent (m)
k	thermal conductivity ($W\,m^{-1}\,K^{-1}$)
K	thermal conductivity ratio, $K = k_s/k_{sub}$
L	substrate thickness (m)
R_c	thermal contact resistance ($m^2\,K\,W^{-1}$)
t	time (s)
T	temperature (°C)
x	linear coordinate
y	linear coordinate

Greek symbols

α	thermal diffusivity ($m^2\,s^{-1}$)
γ	$\lambda_n \xi/\sqrt{\Lambda}$
η	$\lambda_n/\sqrt{\Lambda}$
θ	non-dimensional temperature
λ	separation constant (m^{-1})
ξ	length ratio, $\xi = L/h$
τ	function dependent on t, only
Λ	thermal diffusivity ratio, $\Lambda = \alpha_{sub}/\alpha_s$
Ψ	function dependent on x, only

Subscripts

i	initial
max	maximum extent
n	number
o	in-flight
s	splat
w	substrate

Superscript

*	non-dimensional variable

increase in temperature – influences impact dynamics. But heating can also evaporate volatile compounds adsorbed on the surface, reducing contact resistance [5,7]. Surface cleaning is the dominant effect at lower surface temperatures, whereas oxidation is more evident at high temperatures [8]. Dhiman and Chandra [9] developed an analytical model to predict when solidification induced splashing would occur and found results to be sensitive to values of thermal contact resistance.

Thermal contact resistance values have been measured directly under millimeter sized droplets of molten metal impacting on flat surfaces by measuring either the splat surface temperature variation using an optical pyrometer [2,10,11], or the transient substrate temperature with thermocouples [8,12]. Contact resistance was determined by selecting values that gave best agreement between predictions from numerical or analytical models and experimentally measured temperature variations.

High-speed, two-color pyrometry has been used to obtain splat temperature variation during impact of plasma-sprayed particles [13–15]. In this method, radiation emitted by the spreading splat is recorded at two different wavelengths; assuming gray-body emission, the splat temperature is calculated from the ratio of the intensities of radiation collected. Cedelle et al. [16] measured the cooling rates of yttria-partially-stabilized zirconia on stainless steel substrates that were preheated to 673 K, and then air-cooled to room temperature and found that the cooling rates of splats on the preheated steel were almost an order of magnitude larger than those on non-heated steel. Belghazi et al. [17] used a two-dimensional analytical conduction model for the heat transfer in a two-layered material to show that the thermal contact resistance between the layers significantly influenced the surface temperature changes at the interface between the two layers. For plasma-sprayed zirconia on stainless steel, Bianchi et al. [18] adjusted the thermal contact resistance values in a numerical model in order to match the experimental cooling rate of zirconia with that of a numerical simulation.

Values of thermal contact resistance between impacting plasma particles and substrates are important in developing realistic simulations [1], and in understanding how changing surface properties affects droplet impact dynamics. We have, as yet, no simple analytical method of deriving thermal contact resistance from splat cooling rates. Also, very few measurements of thermal contact resistance under plasma spraying conditions are available. Accurate thermal contact resistance calculations require knowledge of the splat geometry, which can best be obtained by photographing impacting particles while simultaneously measuring their cooling rate.

The objectives of this study were to (1) measure the cooling rates of plasma-sprayed particles during impact; (2) photograph spreading particles; (3) develop an analytical model to calculate the variation of splat cooling rate with thermal contact resistance; (4) calculate thermal contact resistance between plasma-sprayed particles and glass or metal substrates.

2. Experimental method

Photographs of plasma-sprayed molybdenum and yttria-stabilized zirconia on glass and Inconel 625 were captured by using an experimental assembly similar to that described in detail by McDonald et al. [19] and Mehdizadeh et al. [20] and shown in Fig. 1. A SG100 torch (Praxair Surface Technologies, Indianapolis, IN) was used to melt and accelerate dense, spherical molybdenum (SD152, Osram

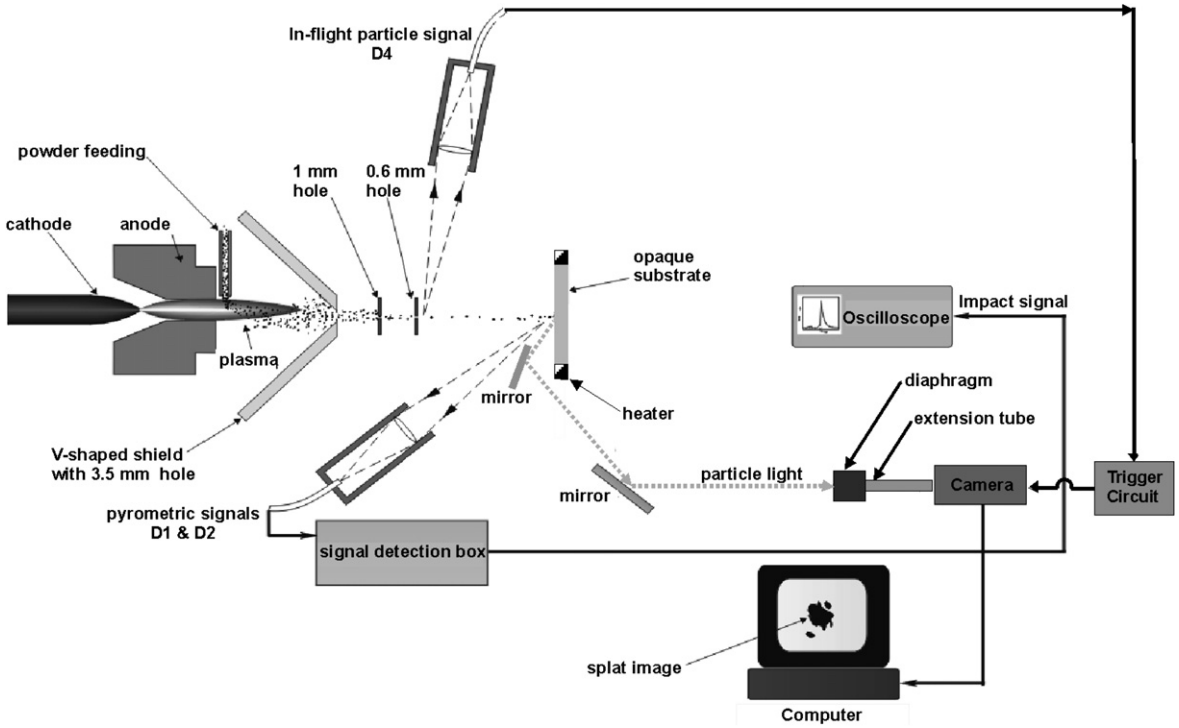

Fig. 1. Schematic of the experimental assembly for impact on Inconel.

Sylvania Chemical and Metallurgical Products, Towanda, PA) and yttria-stabilized zirconia (Amperit #825, H.C. Starck, Germany, referred to as simply "zirconia" in this paper) powder particles, sieved to diameters lying between 38 and 63 μm, with an average diameter of 40 μm. The powder feed rate was less than 1 g/min. The plasma torch was operated with a voltage of 35 V and a current of 700 A. The plasma gas mixture was argon at a flow rate of 50 liters per minute (LPM) and helium at 24.5 LPM, for molybdenum, or 20 LPM, for zirconia. The torch was passed rapidly across the substrates. In order to protect the substrate from an excess of particles and heat, a V-shaped shield was placed in front of the torch (Fig. 1). This V-shaped shield had a 3.5 mm hole through which particles could pass. To reduce the number of particles landing on the substrate, two additional barriers were placed in front of the substrate, the first of which had a 1 mm hole and the second, a 0.6 mm hole. All the holes were aligned to permit passage of the particles with a horizontal trajectory.

The substrates were glass microscope slides (Fisher Scientific, Pittsburgh, PA) that were washed with water and ethanol and dried in an oven at 140 °C for 30 min. In order to heat the substrate, the glass was placed in a copper substrate holder that included resistance heater wires. Mirror-polished Inconel 625 (referred to as simply "Inconel" in this paper) was also used as a substrate. Samples of Inconel were either held at room temperature (non-heated), heated to 400 °C (heated), or pre-heated to 400 °C for 3 h, then air-cooled to room temperature, before spraying the particles.

The thermal radiation of the particle and splat were measured to calculate the in-flight particle temperature and temperature evolution of the splat. A rapid two-color pyrometric system was used to measure the thermal radiation. The system included an optical sensor head that consisted of a custom-made lens that focused the collected radiation, with 0.21 magnification, onto an optical fiber with an 800 μm core [14]. Fig. 2 shows a schematic of the cross-section of the optical fiber and a typical signal obtained from the pyrometric system. The optical fiber was covered with an optical mask that was opaque to near infrared radiation, except for three slits (see Fig. 2(a)). The two smaller slits (slits *b* and *c* in Fig. 2(a)), with dimensions of 30 μm by 150 μm and 30 μm by 300 μm, were used to detect the thermal radiation of the in-flight particles. The radiation was used to calculate the temperature of the in-flight particle [15]. The largest slit (slit *e* in Fig. 2(a)), measuring 150 μm by 300 μm, was used to collect thermal radiation of the particle as it impacted and spread on the substrate.

The collected thermal radiation was transmitted through the optical fiber to a detection unit that contained optical filters and two photodetectors. The radiation beam was divided into two equal parts by a beam splitter. Each signal was transmitted through a bandpass filter with wavelength of either 785 nm or 995 nm and then detected using a silicon avalanche photodetector (model C30817, RCA, Durant, OK). The photodetector had a response time smaller than 0.1 μs [14]. The ratio of the radiation intensity at the chosen wavelengths (referred to as D_1 and D_2, respectively) was used to calculate the particle and splat temperatures with an accuracy of ±100 °C [15].

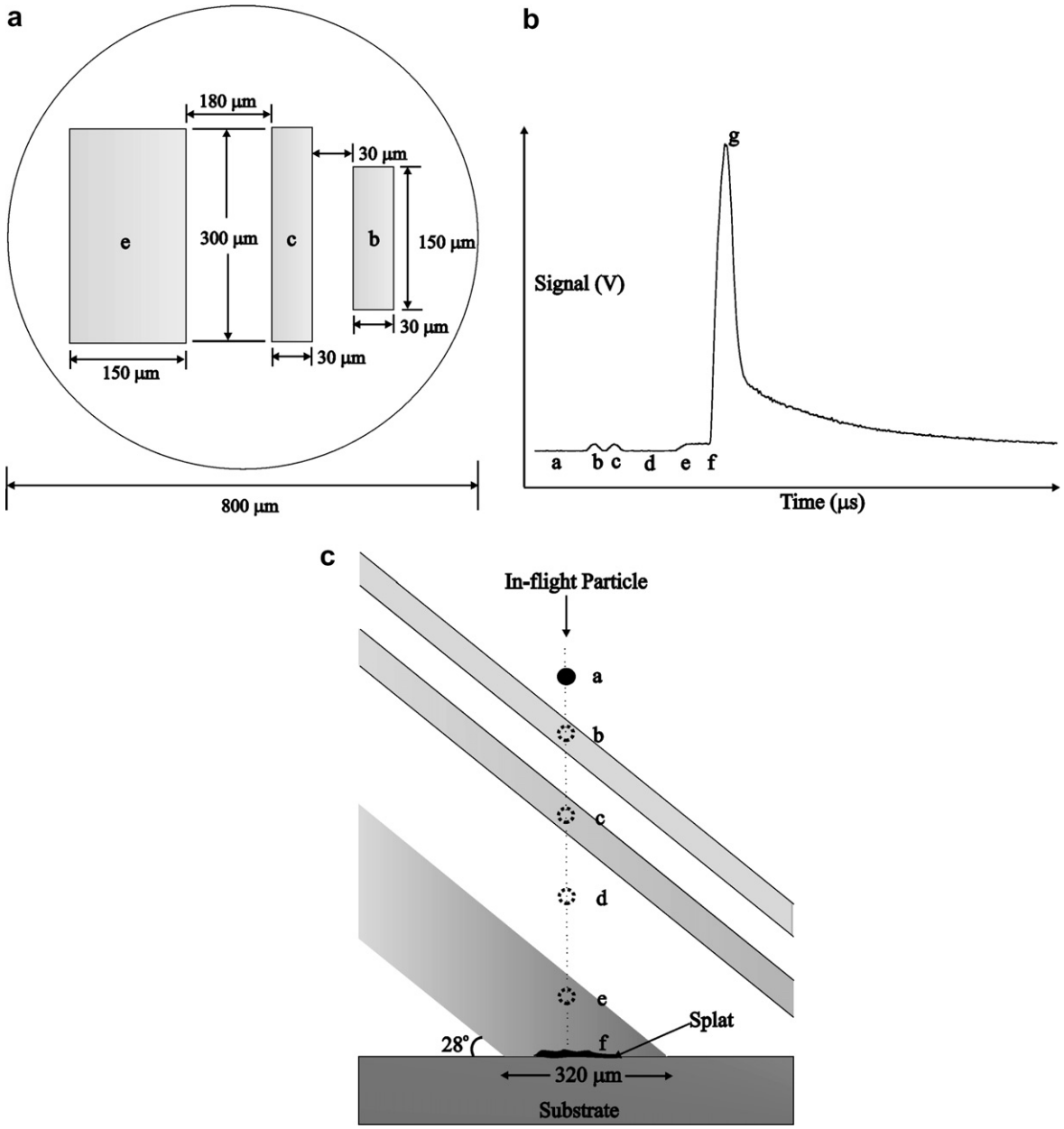

Fig. 2. (a) Details of the three-slit mask, (b) a typical signal collected by the three-slit mask, (c) schematic of the optical detector fields of view.

Fig. 2(b) shows a typical signal captured by a photodetector. The labels, *a–f*, correspond to the position of a particle (shown in Fig. 2(c)) as it passed through the fields of view of each of the optical slits. At points *a* and *d*, the particle was not in the optical field of view of any of the slits, so the signal voltage was zero. The two peaks at points *b* and *c* were produced by thermal emissions from the particle as it passed through the first two small slits. At point *e* the droplet entered the field of view of the third and largest optical slit. This is shown on the thermal signal by a plateau in the profile. Upon impact at *f*, the signal increased as the particle spread and eventually decreased as the particle cooled down and/or splashed out of the field of view. At point *g*, the signal is a maximum and this is representative of the splat at the maximum spread extent.

A 12-bit charge-coupled device (CCD) camera (QImaging, Burnaby, BC) was used to capture images of the spreading particles. Photographs on Inconel were captured from the front of the substrate with the camera attached to a 30 cm long optical extension tube that was connected through a diaphragm (Tominon, Waltam, MA) to a 135-mm focal length lens (Fig. 1). The diaphragm opening diameter was 8.5 mm, corresponding to an aperture of f-16. The shutter of the camera was opened for about 500 μs, with no added illumination. The images obtained were those from the visible radiation emitted by the splats, integrated over the entire droplet impact period. In order to photograph droplets landing on glass, the method described by Mehdizadeh et al. [20] was used. A 5 ns Nd-YAG laser was triggered to illuminate the spreading

droplet, providing a single image of the splat silhouetted against a bright background. By varying the instant at which the laser was pulsed, different stages of droplet impact and spread were captured. The images captured by the camera were digitized by a frame grabber and recorded on a personal computer.

3. Mathematical model

A one-dimensional heat conduction model, in rectangular co-ordinates, was used to calculate thermal contact resistance. Fig. 3 shows a schematic of the model used in the analysis. The liquid splat at its maximum extent, prior to solidification or disintegration, was modelled as a disk transferring heat to the substrate. It was assumed that thermal contact resistance between the splat and the substrate was constant; the thickness of the splat (h) was uniform; convection and radiation were small so that the top and sides of the splat were modelled as being insulated and heat loss from the splat was solely by one-dimensional conduction to the substrate; and all properties were independent of temperature. The splat at the maximum extent and the substrate are assumed to be a two-layered composite solid with a thermal contact resistance between the layers.

The non-dimensionalized governing equations of the temperature distribution in the splat and substrate are

$$\frac{\partial^2\theta_s}{\partial x^{*2}} = \frac{\partial\theta_s}{\partial t^*}, \quad 0 < x^* < 1, \tag{1}$$

$$\frac{\partial^2\theta_w}{\partial x^{*2}} = \frac{1}{\Lambda}\frac{\partial\theta_w}{\partial t^*}, \quad 1 < x^* < \xi. \tag{2}$$

The following variables were used to non-dimensionalize the governing equations:

$$\theta = \frac{T - T_{i,w}}{T_{i,s} - T_{i,w}}, \quad x^* = \frac{x}{h}, \quad t^* = Fo = \frac{\alpha_s t}{h^2},$$
$$\Lambda = \frac{\alpha_w}{\alpha_s}, \quad \xi = \frac{L}{h}. \tag{3}$$

The non-dimensional boundary and initial conditions are

$$\frac{\partial\theta_s}{\partial x^*} = 0, \quad x^* = 0, \tag{4}$$

$$\theta_w = 0, \quad x^* = \xi, \tag{5}$$

$$K\frac{\partial\theta_s}{\partial x^*} = \frac{\partial\theta_w}{\partial x^*}, \quad x^* = 1, \tag{6}$$

$$\frac{\partial\theta_s}{\partial x^*} + Bi(\theta_s - \theta_w) = 0, \quad x^* = 1, \tag{7}$$

$$\theta_s = 1, \quad t^* = 0, \tag{8}$$

$$\theta_w = 0, \quad t^* = 0. \tag{9}$$

K (k_s/k_w) and Bi ($h/R_c k_s$) are the thermal conductivity ratio and the Biot number, respectively. The boundary condition of Eq. (5) states that the temperature of the substrate bottom surface is constant and equal to the initial temperature, since the substrate is large compared to the splat. The boundary conditions of Eqs. (6) and (7) show that the temperature distributions in the splat and substrate are coupled.

The governing equations of the temperature distribution in the splat and substrate (Eqs. (1) and (2)) were solved by the orthogonal expansion technique [21]. This technique is used to derive the temperature distribution in each layer of a multi-layer composite solid by employing the separation of variables method. The solution for $\theta(x^*, t^*)$, was assumed to be the product of two functions, one (Ψ) depending on x^* only, and the other, (τ), on t^* only, so that

$$\theta_s(x^*, t^*) = \Psi_s(x^*)\tau(t^*), \tag{10}$$

$$\theta_w(x^*, t^*) = \Psi_{sub}(x^*)\tau(t^*). \tag{11}$$

Eqs. (10) and (11) were substituted into Eqs. (1) and (2), respectively, and after separation we obtain,

$$\frac{d^2\Psi_{s,n}}{dx^{*2}} + \lambda_n^2\Psi_{s,n} = 0, \tag{12}$$

$$\frac{d\tau_n}{dt^*} + \lambda_n^2\tau_n = 0, \tag{13}$$

$$\frac{d^2\Psi_{w,n}}{dx^{*2}} + \frac{\lambda_n^2}{\Lambda}\Psi_{w,n} = 0. \tag{14}$$

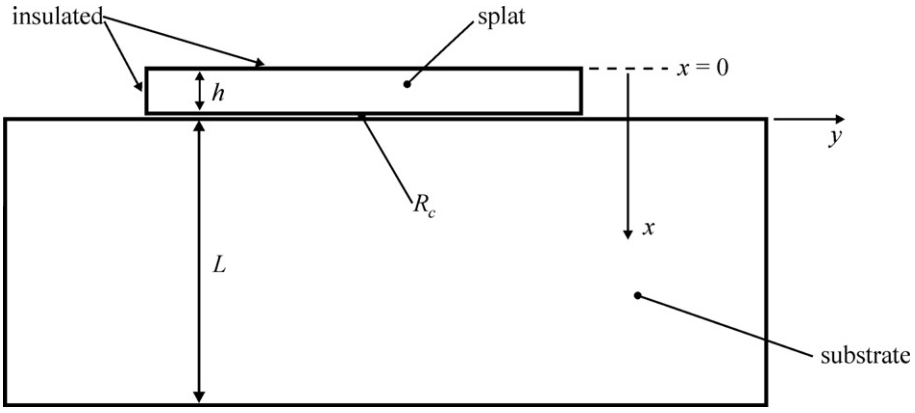

Fig. 3. Schematic of a splat on a surface with thermal contact resistance at the splat–substrate interface.

Eq. (13) is the transient component of the governing equations, and it is the same for both the splat and the substrate. λ_n is the separation constant, which will give the eigenvalues that correspond to the eigenfunctions, Ψ_n.

Integration of Eqs. (12)–(14) gives

$$\Psi_{s,n}(x^*) = A_n \sin(\lambda_n x^*) + B_n \cos(\lambda_n x^*), \tag{15}$$

$$\tau_n(t^*) = G_n \exp(-\lambda_n^2 t^*), \tag{16}$$

$$\Psi_{w,n}(x^*) = C_n \sin\left(\frac{\lambda_n x^*}{\sqrt{\Lambda}}\right) + D_n \cos\left(\frac{\lambda_n x^*}{\sqrt{\Lambda}}\right), \tag{17}$$

where A_n, B_n, C_n, D_n, and G_n are integration constants.

Application of the boundary condition at $x^* = 0$ (Eq. (4)) to Eq. (15) gives $A_n = 0$. The boundary conditions of Eqs. (5)–(7) are applied to Eqs. (15) and (17) in order to find the integration constants.

$$C_n \sin\left(\frac{\lambda_n \xi}{\sqrt{\Lambda}}\right) + D_n \cos\left(\frac{\lambda_n \xi}{\sqrt{\Lambda}}\right) = 0, \tag{18}$$

$$B_n K \lambda_n \sin(\lambda_n) + C_n \left[\frac{\lambda_n}{\sqrt{\Lambda}} \cos\left(\frac{\lambda_n}{\sqrt{\Lambda}}\right)\right] - D_n \left[\frac{\lambda_n}{\sqrt{\Lambda}} \sin\left(\frac{\lambda_n}{\sqrt{\Lambda}}\right)\right] = 0, \tag{19}$$

$$B_n \left[\cos(\lambda_n) - \frac{\lambda_n \sin(\lambda_n)}{Bi}\right] - C_n \sin\left(\frac{\lambda_n}{\sqrt{\Lambda}}\right) - D_n \cos\left(\frac{\lambda_n}{\sqrt{\Lambda}}\right) = 0. \tag{20}$$

Eqs. (18)–(20) are a system of equations that can be used to solve for the constants of integration. Since these equations are homogeneous, the constants can be determined only in terms of one of them. C_n and D_n will be solved in terms of B_n (the non-vanishing constant), so $c_n = C_n/B_n$ and $d_n = D_n/B_n$. Rearrangement of Eqs. (19) and (20) gives c_n and d_n:

$$c_n = \sin\left(\frac{\lambda_n}{\sqrt{\Lambda}}\right)\left[\cos(\lambda_n) - \frac{\lambda_n \sin(\lambda_n)}{Bi}\right] - K\sqrt{\Lambda}\sin(\lambda_n)\cos\left(\frac{\lambda_n}{\sqrt{\Lambda}}\right), \tag{21}$$

$$d_n = \cos\left(\frac{\lambda_n}{\sqrt{\Lambda}}\right)\left[\cos(\lambda_n) - \frac{\lambda_n \sin(\lambda_n)}{Bi}\right] + K\sqrt{\Lambda}\sin(\lambda_n)\sin\left(\frac{\lambda_n}{\sqrt{\Lambda}}\right). \tag{22}$$

The system of homogenous equations, Eqs. (18)–(20), has a non-trivial solution, so the determinant of the coefficients of the constants of integration in Eqs. (18)–(20) will be zero [21]. Solving for the determinant gives an implicit expression for λ_n:

$$K\lambda_n \sin(\lambda_n)[\sin(\gamma)\cos(\eta) - \sin(\eta)\cos(\gamma)] - \eta\left[\cos(\lambda_n) - \frac{\lambda_n \sin(\lambda_n)}{Bi}\right][\sin(\gamma)\sin(\eta) + \cos(\gamma)\cos(\eta)] = 0, \tag{23}$$

where $\gamma = \lambda_n \xi/\sqrt{\Lambda}$ and $\eta = \lambda_n/\sqrt{\Lambda}$.

Since Eqs. (12) and (14) are Sturm–Liuoville equations and the boundary conditions of Eqs. (4)–(7) are homogeneous, orthogonality can be applied to determine G_n [21]. The initial conditions of Eqs. (8) and (9) were used. The resulting expression is integrated from $x^* = 0$ to $x^* = 1$ for the splat and from $x^* = 1$ to $x^* = \xi$ for the substrate:

$$K\Lambda \int_0^1 \Psi_{s,n}(x^*)\,dx = G_n\left[K\Lambda \int_0^1 \Psi_{s,n}^2(x^*)\,dx + \int_1^\xi \Psi_{w,n}^2(x^*)\,dx\right]. \tag{24}$$

Substituting the expressions for $\Psi_{s,n}(x^*)$ and $\Psi_{w,n}(x^*)$ from Eqs. (15) and (17) into Eq. (24) and solving, gives the expression for G_n:

$$G_n = 2K\sqrt{\Lambda}\sin(\lambda_n) * \Big[K\sqrt{\Lambda}[\lambda_n + \sin\lambda_n \cos\lambda_n] + c_n^2[\gamma - \eta - \cos\gamma\sin\gamma + \cos\eta\sin\eta] + 2c_n d_n[\cos^2\eta - \cos^2\gamma] + d_n^2[\gamma - \eta + \cos\gamma\sin\gamma - \cos\eta\sin\eta]\Big]^{-1}. \tag{25}$$

The non-dimensional splat temperature distribution is found by substituting Eqs. (15) and (16) into Eq. (10) and summing to give

$$\theta_s(x^*, t^*) = \sum_{n=1}^{\infty} G_n \exp(-\lambda_n^2 t^*)\cos\lambda_n x^*, \quad 0 < x^* < 1. \tag{26}$$

The thermal emission signals of the splat will permit calculation of the experimental splat temperature evolution and the cooling rate at the top surface of the splat. Eq. (26) was differentiated with respect to t^* to give an expression for the non-dimensional cooling rate at the top surface of the splat ($x = x^* = 0$ in Fig. 3):

$$\frac{\partial\theta_s(0,t^*)}{\partial t^*} = -\sum_{n=1}^{\infty} G_n \lambda_n^2 \exp(-\lambda_n^2 t^*). \tag{27}$$

The non-dimensional cooling rate depends only on the non-dimensional time (Fourier number), the thermal diffusivity ratio ($\Lambda = \alpha_w/\alpha_s$), the thermal conductivity ratio ($K = k_s/k_w$), the length ratio ($\xi = L/h$), and the Biot number ($Bi = h/R_c k_s$). Charts of the non-dimensional cooling rate versus the Biot number can be prepared for different values of the ratio of the product ($\Lambda K\xi$) of the thermal diffusivity ratio, the thermal conductivity ratio, and the length ratio to the non-dimensional time (t^*). The dimensional form of the ratio is

$$\frac{\Lambda K \xi}{t^*} = \frac{\alpha_w k_s L h}{\alpha_s^2 k_w t}. \tag{28}$$

The experimental splat surface cooling rates can be non-dimensionalized by using

$$\frac{\partial\theta_s(0,t^*)}{\partial t^*} = \frac{h^2}{\alpha_s(T_{i,s} - T_{i,w})}\frac{\partial T_s(0,t)}{\partial t}. \tag{29}$$

A MATLAB (MathWorks, Inc., Natick, MA, USA) code was used to solve the implicit expression for λ_n (Eq. (23)) and to find the constants of integration (Eqs. (21), (22) and (25)). Terms in the infinite series of the temperature distribution and cooling rate expressions (Eqs. (26) and

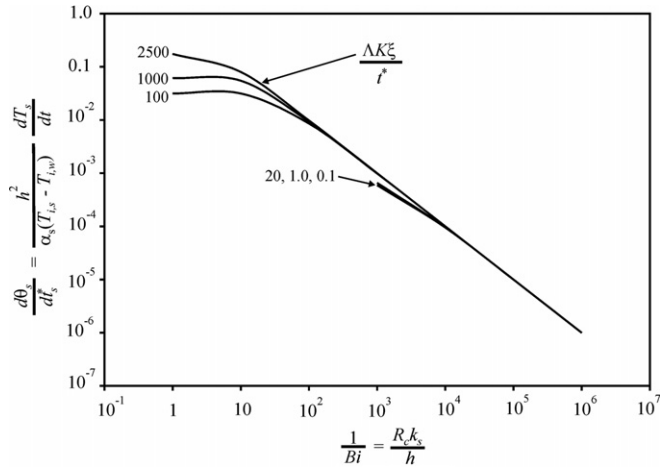

Fig. 4. Log–log plots of the non-dimensional cooling rate versus the inverse Biot number for $10^{-1} \leqslant \frac{1}{Bi} \leqslant 10^{6}$.

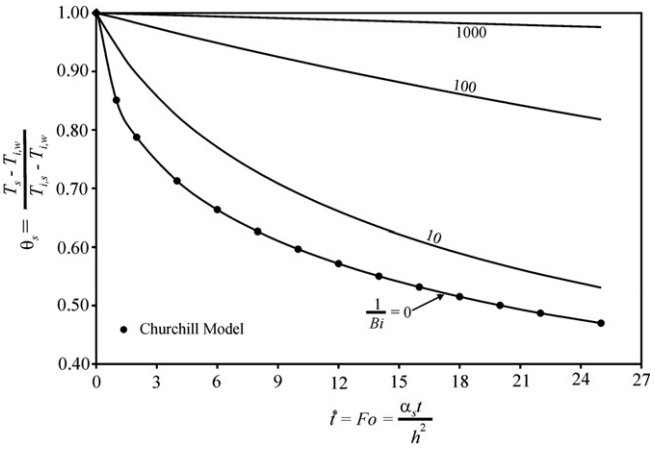

Fig. 5. Variation of non-dimensional temperature with Fourier number for $\Lambda K\xi = 6730$ and different values of the inverse Biot number. Data points show predictions from the model of Churchill for $R_c = 0$ [22].

(27), respectively) were added until the solutions converged to within 1% of the sum.

Fig. 4 shows the variation of the non-dimensional cooling rate ($\partial\theta_s/\partial t^*$) with inverse Biot number ($1/Bi$), for different values of the ratio of the product of the thermal diffusivity ratio, the thermal conductivity ratio, and the length ratio to the non-dimensional time ($\Lambda K\xi/t^*$). The inverse Biot number ($R_c k_s/h$) compares the magnitude of the thermal resistance between the splat and substrate (R_c) to the thermal resistance of the splat itself (h/k_s). As this ratio becomes very large ($>10^4$), heat transfer from the upper splat surface depends largely on R_c, and is independent of properties and splat thickness ($\xi = L/h$); curves with different $\Lambda K\xi/t^*$ values merge with each other (see Fig. 4). In this study, for plasma-sprayed zirconia and molybdenum particles impacting on unheated glass and Inconel surfaces, typically $\partial\theta_s/\partial t^* < 10^{-3}$ and $Bi^{-1} > 10^3$. The impact of plasma-sprayed particles on heated surfaces gave $\partial\theta_s/\partial t^* > 10^{-2}$ and $Bi^{-1} < 10^2$. The cooling rate decreased with increasing thermal contact resistance, approaching zero as Bi^{-1} approached infinity.

Churchill [22] used Laplace transforms to solve Eqs. (1)–(9) for the limiting case of perfect thermal contact. When $R_c = 0$, the non-dimensional temperature at the top surface of the splat is

$$\theta_{\text{Churchill}}(0, t^*) = 1 - (1-\beta)\sum_{n=0}^{\infty}\beta^n \operatorname{erfc}\left[\frac{(2n+1)}{\sqrt{4t^*}}\right], \qquad (30)$$

where

$$\beta = \frac{k_s\sqrt{\alpha_w} - k_w\sqrt{\alpha_s}}{k_s\sqrt{\alpha_w} + k_w\sqrt{\alpha_s}}.$$

Fig. 5 shows that as the inverse Biot number and the thermal contact resistance decrease to zero, the temperatures predicted by Eq. (26) agree well with the predictions of Churchill's model and Eq. (30).

4. Results and discussion

Previous publications [4,19,20,23] have described how splats of molybdenum and zirconia, have been photographed at intervals of a few microseconds during spreading, on both unheated and heated glass surfaces. Fig. 6(a) shows images of plasma-sprayed molybdenum splats impacting on glass at room temperature. The three frames, respectively, show a splat at the maximum spread extent, at the time when splat fragmentation begins, and the remnants of the particle on the substrate after spreading and solidification. Note that each photograph is of a different particle. Fig. 6(b) is the particle thermal emission signal, obtained from radiation falling on the D_1 (785 nm) sensor. The maximum voltage on the profile corresponds to the time when the splat was at the maximum spread diameter, which averaged 370 ± 20 μm. Spread diameters were obtained using the ImageJ imaging software (National Institutes of Health, Washington, DC), which measured the cross-sectional area (A) of the splat at the maximum extent, before break-up, permitting the calculation of a diameter, $D_{\max} = \sqrt{4A/\pi}$. The statistical error, calculated by dividing the standard deviation by the square-root of the number of samples [24], is shown with the average of the diameter. The statistical errors will be shown with all averages in this study.

On the thermal emission signal are marked the instants of particle impact and when the splat reaches its maximum extent (Fig. 6(b)). The cooling curve of Fig. 6(c) shows the splat temperature at the maximum extent ($T_{s,\max}$) and the splat cooling rate at the top surface (dT/dt), measured at the maximum spread extent by calculating the slope of the straight line originating from this point. The initial temperature of the splat in the model ($T_{i,s}$) will be the temperature at the maximum spread extent ($T_{s,\max}$). The oscillatory patterns observed on the temperature profile (Fig. 6(c)) were most likely due to noise. Higher temperatures will produce stronger signals, increasing the signal

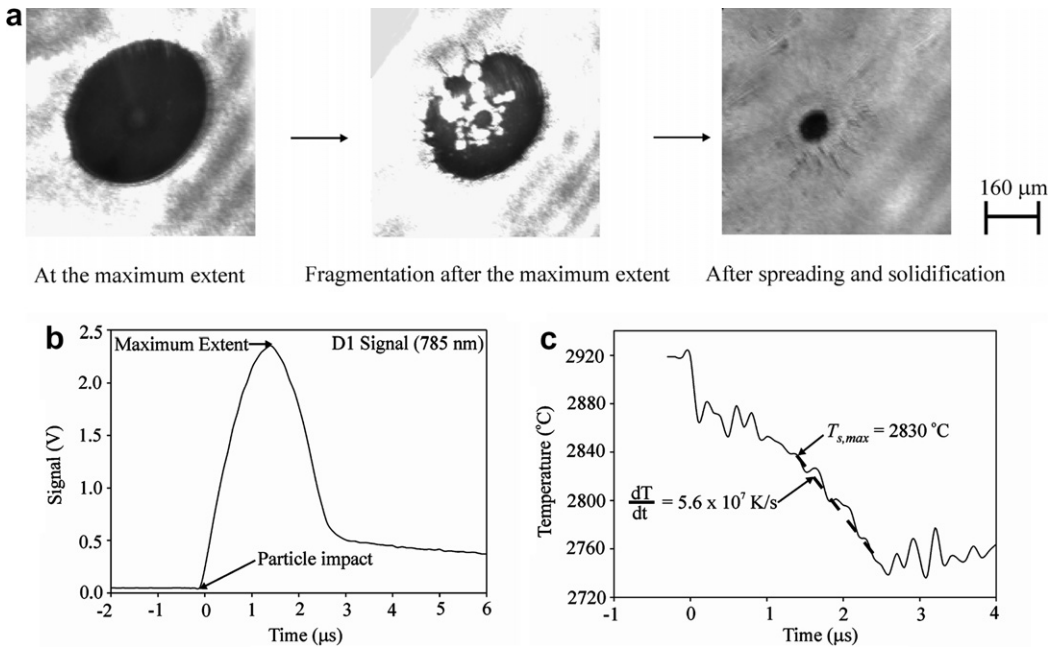

Fig. 6. (a) Images, (b) a typical thermal emission signal, and (c) a typical cooling curve of molybdenum splats on glass held at room temperature.

Table 1
Experimental average splat temperatures at the maximum extent and cooling rates on non-heated substrates

Material/substrate	$T_{s,max}$ (°C)	dT/dt (K/s ($\times 10^{-7}$))
Mo/glass	2830 ± 20	5.6 ± 0.5
Mo/Inconel	2680 ± 20	12 ± 0.5
Zirconia/glass	2800 ± 30	13 ± 2.0

to noise ratio, and reducing the observed oscillations. It has been shown that, in general, the accuracy of temperature measurements obtained by the two-color pyrometry method is ±100 °C [15]. Table 1 shows average values of the experimental temperatures at the maximum extent and the experimental cooling rate of molybdenum on non-heated glass.

Fig. 7 shows impact images, a typical thermal emission signal, and a cooling curve of plasma-sprayed zirconia on non-heated glass. The images (Fig. 7(a)) show that the spreading and fragmentation dynamics of zirconia are similar to those of molybdenum, except that splat fragmen-

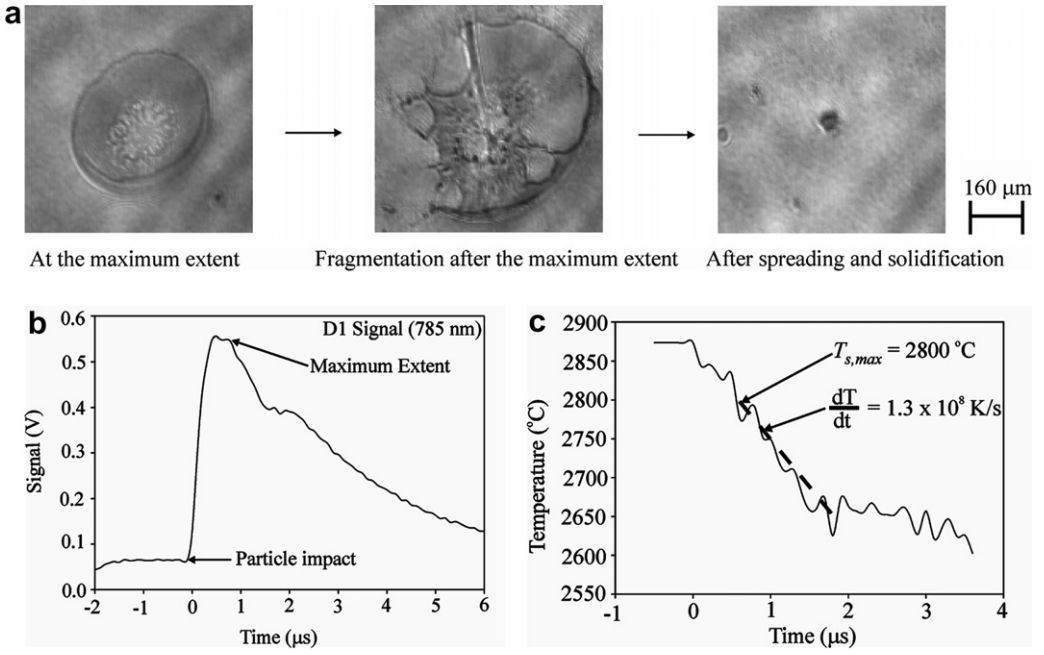

Fig. 7. (a) Images, (b) a typical thermal emission signal, and (c) a typical cooling curve of yttria-stabilized zirconia splats on glass held at room temperature.

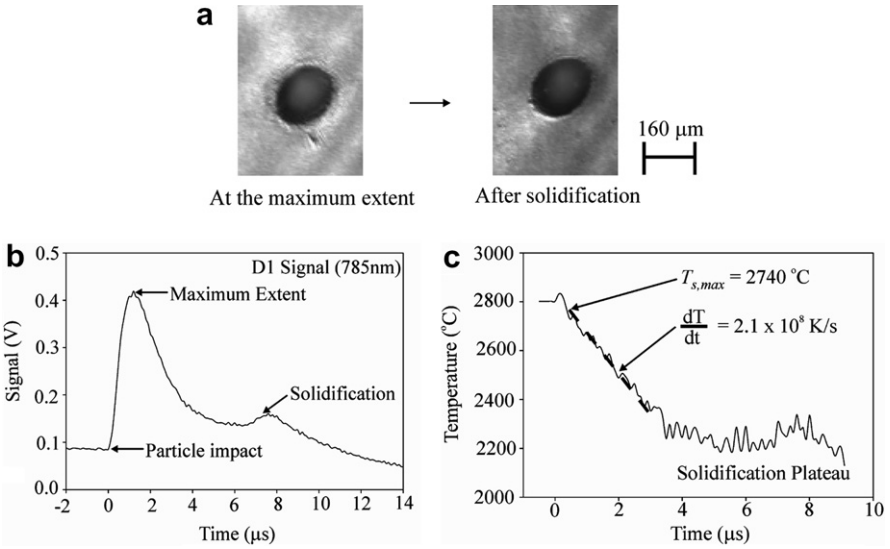

Fig. 8. (a) Images, (b) a typical thermal emission signal, and (c) a typical cooling curve of molybdenum splats on glass held at 400 °C.

tation appears even more pronounced. The particles spread to an average maximum diameter of about 460 ± 20 μm and fragment, leaving a central solidified core. Table 1 and the cooling curve of Fig. 7(c) show the average temperature at the maximum extent and the average cooling rate of zirconia on non-heated glass.

Heating the substrate produced significant changes in both particle impact dynamics and heat transfer. Fig. 8 shows plasma-sprayed molybdenum splats impacting on glass heated to 400 °C. Images (Fig. 8(a)) show that splat fragmentation is significantly reduced and the final diameter of the splat after solidification is approximately equal to the maximum spread diameter (130 ± 8 μm). There was little loss of material and the final solid splat was disk shaped. The thermal emission signal (Fig. 8(b)) shows a sudden rise approximately 2.5 μs after the maximum voltage, indicating release of latent heat during solidification. The cooling rate, dT/dt, indicated in Fig. 8(c), was almost an order of magnitude greater than that on a cold glass surface (compare with Fig. 6(c)). When the splat cooling rate was on the order of 10^8 K/s, the solidification plateau was at a temperature (2275 °C) lower than the melting point of molybdenum (2620 °C) (Fig. 8(c)). This could be attributed to undercooling, where the splat began to solidify at a temperature lower than the melting point of the material. It could also be due to errors in the pyrometric readings caused by the assumption that the splat was a gray body. The accuracy of the temperatures obtained by this method was ±100 °C [15]. Lee et al. [25] have shown a mathematical model capable of estimating the rate of heat transfer from droplets on a high temperature wall. Cooling rates obtained by the pyrometric method could be compared to those obtained from the model to test the accuracy of the pyrometric method. Table 2 shows average values of the experimental temperature at the maximum extent and the experimental cooling rate of molybdenum on heated glass.

Table 2
Experimental average splat temperatures at the maximum extent and cooling rates on heated/preheated substrates

Material/substrate	$T_{s,max}$ (°C)	dT/dt (K/s ($\times 10^{-7}$))
Mo/glass	2740 ± 10	21 ± 1.0
Mo/Inconel	2360 ± 30	3.4 ± 4.0
Mo/preheated Inconel	2300 ± 40	22 ± 2.5
Zirconia/glass	2800 ± 15	20 ± 5.0

Heating the glass substrate under plasma-sprayed zirconia particles produced similar changes in impact behavior (Fig. 9). Particles spread after impact on a glass surface at 400 °C to an average maximum diameter of 170 ± 2 μm, without significant fragmentation, and solidified within 2 μs after reaching maximum spread (see Fig. 9(a)). The increase in thermal emission during solidification, seen in Fig. 8(b) for molybdenum, was not observed in Fig. 9(b) for zirconia. Other researchers [26] have previously noted the absence of a solidification peak in the cooling curves for plasma-sprayed zirconia. Molten zirconia is partially transparent [27], which is the reason that images of zirconia splats (Fig. 7(a)) did not have as high a contrast as those of molybdenum (Fig. 6(a)), which is opaque. For the partially-transparent zirconia, thermal sensors receive radiation emitted from some depth within the particle rather than just the surface. Since sensors see not only the solidification front, which is at a constant temperature, but the temperature gradient in the rapidly cooling molten region in front of it, the integrated signal may not show a peak representative of splat solidification. Table 2 shows average values of the temperature at the maximum extent and the cooling rate of zirconia on heated glass.

Fig. 10 shows images of molybdenum splats on Inconel surfaces, both during impact and after solidification. Since impacting particles could not be backlit on the metal substrate, they were photographed with a long camera

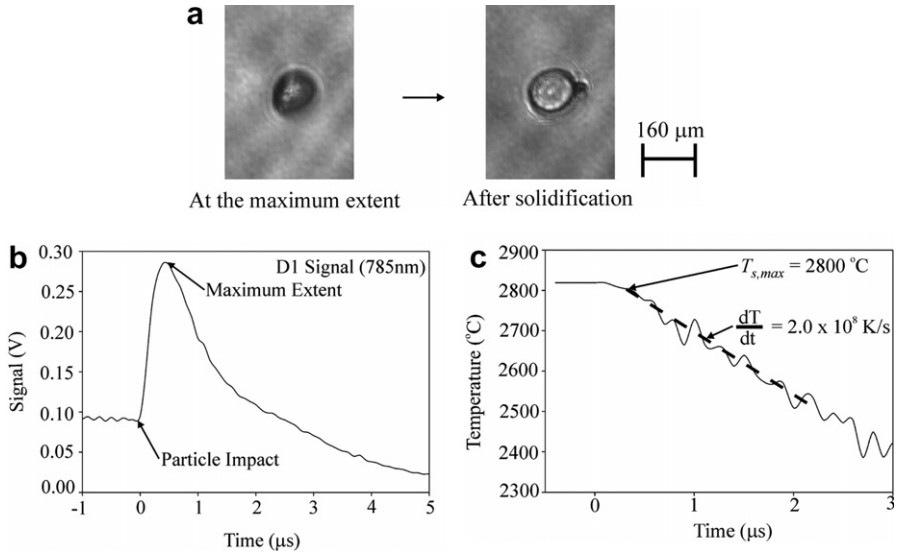

Fig. 9. (a) Images, (b) a typical thermal emission signal, and (c) a typical cooling curve of yttria-stabilized zirconia splats on glass held at 400 °C.

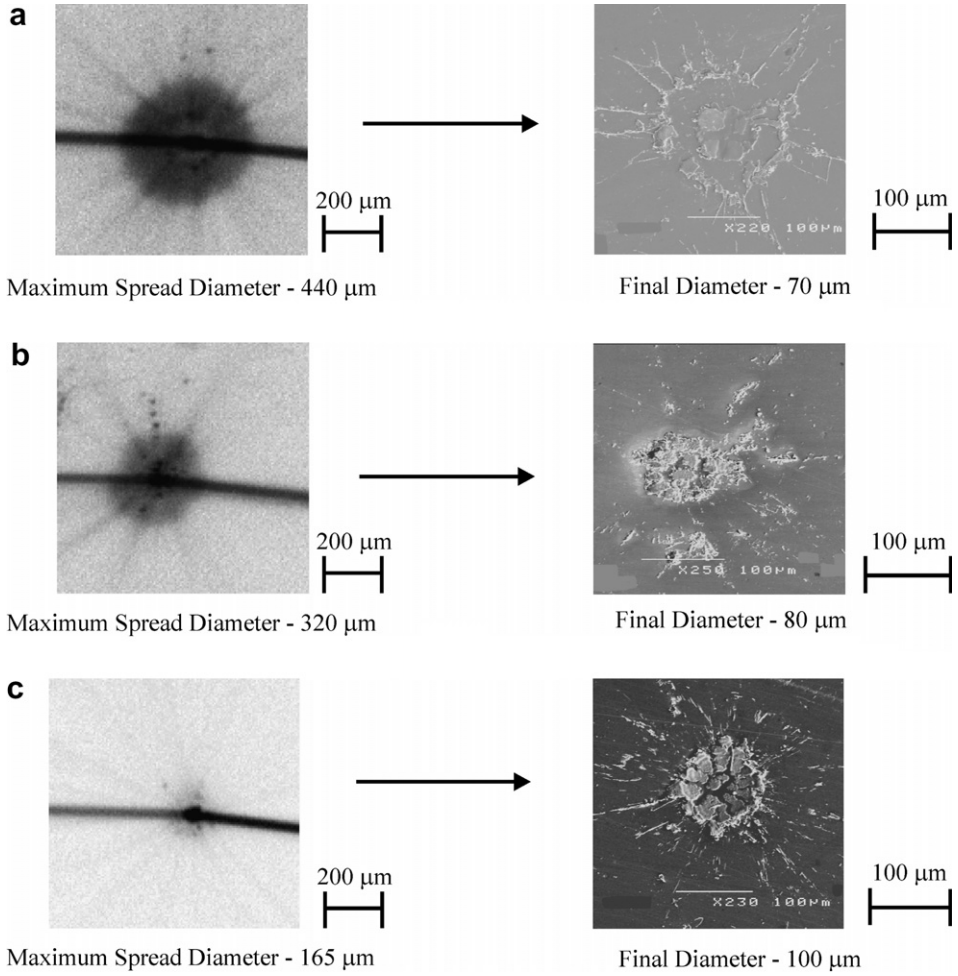

Fig. 10. Images of molybdenum splats at the maximum spread extent and after solidification on Inconel (a) at room temperature, (b) preheated to 400 °C, then air-cooled, and (c) at 400 °C.

exposure time of 500 μs, to produce images that present an integrated view of their entire motion. Two black streaks appear in the images, radiating from the centre of the splat. The streak on the right represents the path of the in-flight

particle and the other, its reflection in the mirror-polished Inconel. The images after impact are SEM micrographs of the portion of splats that remained adhering to the surface. On non-heated Inconel (Fig. 10(a)) splats spread to an average maximum diameter of 440 ± 10 μm and, after significant fragmentation, the average diameter of the splat on the surface was 70 ± 3 μm. The final diameter measured was that of the central portion of the splat that remained mostly intact, excluding the ring of debris and long fingers formed due to splashing. Fragmentation was slightly reduced on the preheated Inconel (Fig. 10(b)), that was heated to 400 °C for 3 h, then air-cooled to room temperature before spraying. On this surface, the splats spread to an average maximum diameter of 320 ± 30 μm, with an average final diameter of 80 ± 3 μm. Fragmentation was further reduced on the heated Inconel surface (Fig. 10(c)); the average maximum spread diameter was 165 ± 10 μm and the average final splat diameter was 100 ± 5 μm. The cooling rates of the splats on the three substrates are listed in Tables 1 and 2. The highest cooling rate was on heated, and the lowest on unheated Inconel, with an intermediate value on the preheated surface. The brightness of the splat images in Fig. 10 reflects their cooling rate: the brightest image corresponds to the lowest cooling rate, since the splat remained hot for a longer time.

Thermal contact resistance was calculated from measurements of cooling rate and splat temperatures listed in Tables 1 and 2, using either the chart of Fig. 4, or, for greater accuracy, Eq. (27) and the constants of Eqs. (21)–(23) and (25). Any time period before splat solidification or fragmentation may be used. Thermophysical properties of splats and substrates [28–33] are shown in Table 3. Conservation of volume between the in-flight droplet (a sphere of diameter D_o) and the splat at the maximum extent (assumed to be a cylindrical disk of thickness h and diameter D_{max}) gives an expression for the splat thickness:

$$h = \frac{2D_o^3}{3D_{max}^2}. \tag{31}$$

The thickness of splats on heated surfaces was larger (~2 μm) than those on unheated surfaces (~0.5 μm).

Table 4 shows calculated values of thermal contact resistances between plasma-sprayed molybdenum and zirconia splats on either glass or Inconel substrates. On all substrates heated to 400 °C, thermal contact resistances were one or two orders of magnitude lower ($R_c \sim 10^{-7}$–10^{-6} m^2K/s) than those on non-heated surfaces ($R_c \sim 10^{-5}$ m^2K/s). Preheating Inconel substrates for 3 h at 400 °C, then air-cooling to room temperature, reduced the thermal contact resistance by one order of magnitude ($R_c \sim 10^{-6}$ m^2K/s). The order of magnitude of the thermal contact resistances on each surface is within the range previously determined by Bianchi et al. [18].

Table 3
Thermophysical properties used in the model

Material	Melting point (°C)	α (m^2/s)	k (W/mK)
Molybdenum	2617	1.9×10^{-5}	72 [28,29]
Zirconia	2700	6.6×10^{-7}	3.8 [27]
Substrate	**Temperature (°C)**		
Glass	27	1.9×10^{-6}	4.0 [31]
	400	1.2×10^{-6}	3.3 [31]
Inconel	27	2.7×10^{-6}	9.8 [32]
	400	4.2×10^{-6}	17.6 [32]

Table 4
Thermal contact resistances between the splats and various substrates

Material/substrate	Substrate temperature (°C)	R_c (m^2K/W ($\times 10^7$))
Mo/glass	27	490 ± 55
	400	6.5 ± 1.0
Mo/Inconel	27	190 ± 15
	400	12 ± 2.0
	Preheated; 27	55 ± 10
Zirconia/glass	27	220 ± 30
	400	10 ± 3.0

Thermal contact resistance between an impacting particle and a non-heated solid substrate has been attributed to the presence of volatile compounds on the surface, which evaporate under the hot splat and form a gaseous barrier between the two surfaces [2,5,34,35]. On heated or preheated surfaces, these adsorbates/condensates are almost completely vaporized [2,5,7,36], improving splat–substrate contact and greatly reducing the thermal contact resistance at the splat–substrate interface. Prolonged heating of a metallic substrate, however, leads to the formation of an oxide layer [6,37], which may lead to increased thermal contact resistance as the thickness of the oxide layer increases. Prolonged heating of glass did not change the thermal contact resistance significantly, since heating does not promote further oxidation on glass. The thermal contact resistance between glass heated for 3 h, then air-cooled to room temperature and molybdenum splats was the same as that between non-heated glass and the splats.

5. Conclusions

The effect of substrate heating on the thermal contact resistance between plasma-sprayed particles and the substrate was studied. The particles that impacted on heated or preheated surfaces had larger cooling rates, smaller maximum spread diameters, and significantly reduced fragmentation, compared to particles that impacted non-heated surfaces.

An analytical, one-dimensional heat conduction model was developed to determine thermal contact resistance, in which the liquid splat at its maximum extent was assumed to be a disk transferring heat to the substrate. Charts were presented showing variation of the non-dimensional cooling rate with inverse Biot number. Thermal contact resistance between heated surfaces and splats was more than an order of magnitude smaller than that between unheated surface and splats. On a preheated surface, the thermal

contact resistance was an order of magnitude smaller. These observations supported the hypothesis that reduction of splat fragmentation and maximum spread diameter, due to larger cooling rates and more rapid solidification on the heated and preheated surfaces, can be attributed to low thermal contact resistance at the splat–surface interface.

Acknowledgments

The authors gratefully acknowledge the technical assistance of M. Lamontagne with assembly of the experimental apparatus and operation of the plasma-spraying equipment and A. Pourmousa for assistance with the MATLAB software. Funding for this project was provided by the Natural Sciences and Engineering Research Council of Canada (NSERC).

References

[1] M. Pasandideh-Fard, V. Pershin, S. Chandra, J. Mostaghimi, Splat shapes in a thermal spray coating process: simulations and experiments, J. Therm. Spray Technol. 11 (2002) 206–217.
[2] M. Fukumoto, E. Nishioka, T. Matsubara, Flattening and solidification behavior of a metal droplet on a flat substrate surface held at various temperatures, Surf. Coat. Technol. 120/121 (1999) 131–137.
[3] S. Costil, H. Liao, A. Gammoudi, C. Coddet, Influence of surface laser cleaning combined with substrate preheating on the splat morphology, J. Therm. Spray Technol. 14 (2005) 31–38.
[4] A. McDonald, M. Lamontagne, C. Moreau, S. Chandra, Visualization of impact of plasma-sprayed molybdenum particles on hot and cold glass substrates, in: E. Lugscheider (Ed.), International Thermal Spray Conference, ASM International, Materials Park, OH, 2005, pp. 1192–1197.
[5] X. Jiang, Y. Wan, H. Hermann, S. Sampath, Role of condensates and adsorbates on substrate surface on fragmentation of impinging molten droplets during thermal spray, Thin Solid Films 385 (2001) 132–141.
[6] V. Pershin, M. Lufitha, S. Chandra, J. Mostaghimi, Effect of substrate temperature on adhesion strength of plasma-sprayed nickel coatings, J. Therm. Spray Technol. 12 (2003) 370–376.
[7] C. Li, J. Li, W. Wang, The effect of substrate preheating and surface organic covering on splat formation, in: C. Coddet (Ed.), Thermal Spray: Meeting the Challenges of the 21st Century, ASM International, Materials Park, OH, 1998, pp. 473–480.
[8] Y. Heichal, S. Chandra, Predicting thermal contact resistance between molten metal droplets and a solid surface, J. Heat Transfer 127 (2005) 1269–1275.
[9] R. Dhiman, S. Chandra, Freezing-induced splashing during impact of molten metal droplets with high Weber numbers, Int. J. Heat Mass Transfer 48 (2005) 5625–5638.
[10] W. Liu, G. Wang, E. Matthys, Thermal analysis and measurements for a molten metal drop impacting on a substrate: cooling, solidification and heat transfer coefficient, Int. J. Heat Mass Transfer 38 (1995) 1387–1395.
[11] G. Wang, E. Matthys, Experimental determination of the interfacial heat transfer during cooling and solidification of molten metal droplets impacting on a metallic substrate: effect of roughness and superheat, Int. J. Heat Mass Transfer 45 (2002) 4967–4981.
[12] S. Aziz, S. Chandra, Impact recoil and splashing of molten metal droplets, Int. J. Heat Mass Transfer 43 (2000) 2841–2857.
[13] S. Fantassi, M. Vardelle, A. Vardelle, P. Fauchais, Influence of the velocity of plasma-sprayed particles on splat formation, J. Therm. Spray Technol. 2 (1993) 379–384.
[14] P. Gougeon, C. Moreau, Simultaneous independent measurement of splat diameter and cooling time during impact on a substrate of plasma-sprayed molybdenum particles, J. Therm. Spray Technol. 10 (2001) 76–82.
[15] C. Moreau, P. Cielo, M. Lamontagne, S. Dallaire, M. Vardelle, Impacting particle temperature monitoring during plasma spray deposition, Meas. Sci. Technol. 1 (1990) 807–814.
[16] J. Cedelle, M. Vardelle, P. Fauchais, M. Fukumoto, Thermal behavior at impact of micrometre and millimetre sized particles, influence of substrate roughness and skewness, in: E. Lugscheider (Ed.), International Thermal Spray Conference, ASM International, Materials Park, OH, 2005, pp. 1180–1186.
[17] H. Belghazi, S. Ben Naoua, M. El Ganaoui, P. Fauchais, Solution analytique bidimensionnelle du transfert de chaleur instationnaire dans un matériau bicouche en contact imparfait, in: Congrès Français de Thermique, Societé Française de Thermique, Reims, France, 2005, pp. 1–6 (in French).
[18] L. Bianchi, A. Leger, M. Vardelle, A. Vardelle, P. Fauchais, Splat formation and cooling of plasma-sprayed zirconia, Thin Solid Films 305 (1997) 35–47.
[19] A. McDonald, M. Lamontagne, C. Moreau, S. Chandra, Impact of plasma-sprayed metal particles on hot and cold glass surfaces, Thin Solid Films 514 (2006) 212–222.
[20] N. Mehdizadeh, M. Lamontagne, C. Moreau, S. Chandra, J. Mostaghimi, Photographing impact of molten molybdenum particles in a plasma spray, J. Therm. Spray Technol. 14 (2005) 354–361.
[21] M.N. Özişik, Heat Conduction, second ed., John Wiley and Sons Inc., New York, 1993, pp. 284–309.
[22] R.V. Churchill, Operational Mathematics, third ed., McGraw-Hill Inc., New York, 1972, pp. 155–157.
[23] A. McDonald, M. Lamontagne, C. Moreau, S. Chandra, Photographing impact of plasma-sprayed zirconia and amorphous steel particles on hot and cold glass substrates, in: J. Mostaghimi, T. Coyle, V. Pershin, H. Salimi-Jazi (Eds.), 17th International Symposium on Plasma Chemistry, Plasma Spray, and Thermal Plasma Materials Processing, University of Toronto, Toronto, ON, 2005, pp. 980–986.
[24] J.R. Taylor, An Introduction to Error Analysis: The Study of Uncertainties in Physical Measurements, University Science Books, Mill Valley, CA, 1982, pp. 89.
[25] C. Lee, K. Lee, J. Senda, H. Fujimoto, A study on the spray-wall interaction model considering degree of superheat in the wall surface, Numer. Heat Transfer, Part B 40 (2001) 495–513.
[26] K. Shinoda, Y. Kojima, T. Yoshida, In-situ measurement system for deformation and solidification phenomena of yttria-stabilized zirconia droplets impinging on quartz glass substrate under plasma-spraying conditions, J. Therm. Spray Technol. 14 (2005) 511–517.
[27] L. Dombrovsky, M. Ignatiev, An estimate of the temperature of semitransparent oxide particles in thermal spraying, Heat Transfer Eng. 24 (2003) 60–68.
[28] C. Moreau, M. Lamontagne, P. Cielo, Influence of the coating thickness on the cooling rates of plasma-sprayed particles impinging on a substrate, Surf. Coat. Technol. 53 (1992) 107–114.
[29] E. Brandes, G. Brook, Smithells Metals Reference Book, sixth ed., Butterworth Inc., 1983, pp. 7–14.
[30] V. Zinov'ev, Handbook of Thermophysical Properties of Metals at High Temperatures, Nova Science Publishers Inc., Commack, NY, 1996, pp. 294.
[31] I. Barin, Thermochemical Data of Pure Substances, third ed., vol. II, VCH Publishers Inc., New York, NY, 1995, pp. 917.
[32] Y. Çengel, Heat Transfer: A Practical Approach, second ed., McGraw-Hill Inc., New York, NY, 2003, pp. 861.
[33] High Temp Metals, Inc., Inconel 625 Technical Data, Sylmar, CA, 2006. <www.hightempmetals.com>.
[34] R. McPherson, The relationship between the mechanism of formation, microstructure and properties of plasma-sprayed coatings, Thin Solid Films 83 (1981) 297.
[35] N. Ootsuka, T. Goji Etoh, K. Takehara, S. Oki, Y. Takano, Y. Hatsuki, S. Thoroddsen, Air-bubble entrapment due to a drop, in:

D. Paisley, S. Kleinfelder, D. Snyder, B. Thompson (Eds.), 26th International Congress on High-Speed Photography and Photonics, International Society for Optical Engineering Proceedings 5580, Alexandria, VA, 2004, pp. 153–161.

[36] P. Fauchais, M. Fukumoto, A. Vardelle, M. Vardelle, Knowledge concerning splat formation: an invited review, J. Therm. Spray Technol. 13 (2004) 1–24.

[37] M. Fukumoto, I. Ohgitani, M. Shiiba, T. Yasui, Effect of substrate surface change by heating on transition in flattening behavior of thermal sprayed particles, in: E. Lugscheider, C. Berndt (Eds.), Thermal Spray 2004: Advances in Technology and Application, ASM International, Materials Park, OH, 2004, pp. 1–6.